Available online at www.sciencedirect.com
ScienceDirect
Journal of the European Ceramic Society 28 (2008) 1845–1855
www.elsevier.com/locate/jeurceramsoc

The influence of cooling rate and SiO_2 additions on the grain boundary structure of Mn-doped PTC thermistors

M.A. Zubair, C. Leach *

Materials Science Centre, School of Materials, University of Manchester, Manchester M1 7HS, UK

Received 26 July 2007; received in revised form 11 December 2007; accepted 16 December 2007
Available online 10 March 2008

Abstract

$BaTiO_3$ based positive temperature coefficient of resistance (PTC) thermistors were prepared with 0, 1.0, 2.0 and 3.0 at.% SiO_2 additions. The effects of these SiO_2 additions and cooling rate variations on microstructural development and bulk electrical performance are discussed in the context of the double Schottky barrier (DSB) model. An increase in SiO_2 content increased the proportion of triple junctions containing $BaTiSi_2O_8$, but reduced the density slightly, without affecting the grain size. The bulk charge carrier density was unaffected either by SiO_2 level or changes to the cooling rate. Adding SiO_2 or increasing the post sintering cooling rate decreased ρ_{25} and ρ_{max}, and increased $T\rho_{max}$. These effects were attributed to a reduction in activated surface state density, while maintaining a fixed acceptor energy depth.

By assuming a single acceptor state energy level, satisfactory agreement between theory and experimental PTC behaviour was only obtained at $T\rho_{max}$. Agreement was extended over a wider range of temperatures when the acceptor states were considered to be spread over a broader energy interval.

Keywords: $BaTiO_3$; Grain boundaries; PTC; Thermistors

1. Introduction

Positive temperature coefficient of resistance (PTC) thermistors, based on donor and acceptor co-doped $BaTiO_3$, exhibit an anomalous rise in grain boundary resistivity over a small temperature interval just above the ferro- to para-electric transition temperature, T_C. A mechanism for this process was first proposed by Heywang[1] and subsequently developed by Jonker.[2,3] In this model the sudden increase in grain boundary resistivity above T_C is associated with the formation of a Schottky-type potential barrier within a permittivity-dependant depletion-layer. The barrier is due to filled acceptor traps, formed within a 2D layer of segregated acceptor ions,[4] or adsorbed oxygen[5] at the grain boundaries, and disappears below T_C due to charge compensation by spontaneous polarization. An alternative model for the formation of a permittivity-dependant interfacial potential barrier where cation vacancies, mainly Ba-vacancies, act as acceptors was proposed by Daniels and Wernicke.[6] In their model, samples prepared with an appropriate donor concentration and sintered in an atmosphere containing a suitable oxygen partial pressure form a Ba-vacancy rich insulating layer at the grain boundaries, resulting in an n-i-n type interfacial structure.The resistivity of the depletion-layer, ρ_L, is approximately given by[1,7]:

$$\rho_L = R_0 \exp\left\{\frac{e\varphi_0(T)}{kT}\right\} \quad (1)$$

where, R_0 = constant, e = electronic charge, $\varphi_0(T)$ = height of the potential barrier at temperature T, and k = Boltzmann constant. $\varphi_0(T)$ can be obtained from the solution of the 1D Poisson equation:[8]

$$\varphi_0(T) = \frac{eN_S(T)^2}{8\varepsilon_0\varepsilon_L'(T)N_d} \quad (2)$$

where, $N_S(T)$ = density of occupied acceptor states at temperature T, ε_0 = permittivity of free space, N_d = charge carrier (effective donor) concentration. ε_L' is the relative permittivity of the material within the grain boundary layer, which can be

* Corresponding author. Tel.: +44 161 306 3561; fax: +44 161 306 3586.
E-mail address: colin.leach@manchester.ac.uk (C. Leach).

0955-2219/$ – see front matter © 2008 Elsevier Ltd. All rights reserved.
doi:10.1016/j.jeurceramsoc.2007.12.034

described through the Curie–Weiss law:

$$\varepsilon_{\mathrm{L}}^{/} = \frac{C}{T - T_{\mathrm{C}}} \tag{3}$$

where C = Curie constant.

Addition of 3-d elements, especially Mn, is believed to increase the magnitude of the PTC effect through the formation of deep grain boundary acceptor states.[9] Experimental evidence for segregation of Cu, Fe and Mn to secondary grain boundary phases led early workers to postulate this as an explanation for the observation that only small additions are necessary to achieve a large increase in the magnitude of the overall resistance increase during the PTC transition.[1,10] However, it has also been noted that many transition elements have high solubility limits in $BaTiO_3$, and that only Cu and V are likely to segregate to secondary phases, while others distribute homogeneously throughout the structure.[9]

The n-i-n layer model[6] allows for a homogeneous distribution of acceptor ions throughout the lattice, and assumes the majority of donor states are compensated by Ba-vacancies, reducing the effective donor concentration to a level similar to that of the acceptors. In this model the addition of acceptor levels with higher energies than that of the Ba-vacancy increases the thickness of the insulating layer in the n-i-n structure, increasing the magnitude of the resistivity change during the PTC transition.

In thermistors co-doped with La and Mn, charge neutrality arguments have been used to suggest that diffusion of atmospheric oxygen during cooling generates electron traps, leading to oxidation of Mn-ions at the grain surfaces.[11,12]

SiO_2 and TiO_2 are commonly added as sintering aids.[13,14] SiO_2 and Mn additions are also reported to assist homogenization of the microstructure during sintering, improving the performance of PTC thermistors under transient loads.[15] In terms of electrical properties, the variation of permittivity with temperature is significantly affected by SiO_2 additions: with increasing SiO_2 the permittivity increases below T_{C}, although the permittivity close to the temperature of maximum resistivity, $T\rho_{\max}$, remains almost unchanged.[16] It has been reported that increasing the SiO_2 content in La-doped $BaTiO_3$ initially causes an increase in room temperature resistivity, followed by a sudden decrease. The initial rise was attributed to homogenization of the microstructure through the formation of a liquid phase, and the subsequent decrease to fresnoite formation, which reduced the surface Ba-vacancy concentration by reducing the contact area between intergranular $Ba_6Ti_{17}O_{40}$, and $BaTiO_3$ grains.[17]

In the present study we have systematically analysed resistance–temperature ($\rho(T)$) curves from series of PTC thermistors, formed as a function of cooling rate and SiO_2 content, in the framework of the double Schottky barrier (DSB) model, in order to establish the effect of variations in these process parameters on the electrical structure of the grain boundaries. We have done this through a combination of microstructural studies and extension of an analysis describing the effect of variations in surface state density, N_{SO}, and acceptor level energy, E_{S}, on $\rho(T)$ [18] to include subsequent work, which generalised N_{SO} and E_{S} in $\rho_{\max}$–$T_{\max}$ space[9] and trap energy distributions.[19] These are compared with values obtained through Arrhenius analysis of the same data.[7] We will demonstrate that SiO_2 additions systematically alter the low field $\rho(T)$ characteristics of PTC thermistors above T_{C} in a manner directly analogous to changes in cooling rate.

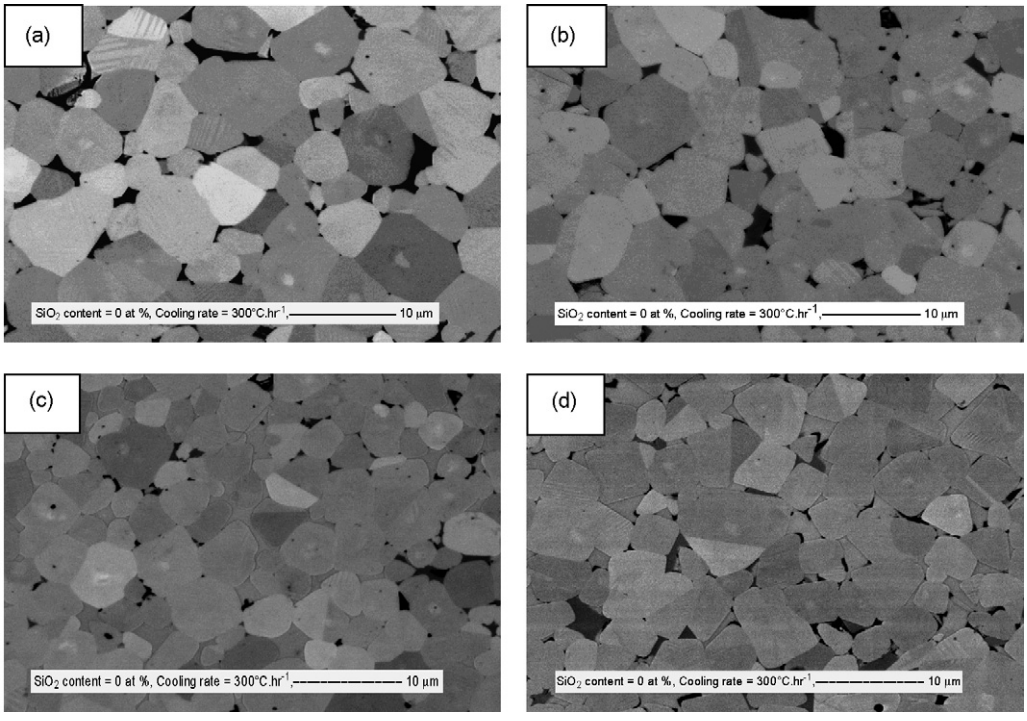

Fig. 1. Backscattered electron images of samples with (a) 0 at.% SiO_2, (b) 1.0 at.% SiO_2, (c) 2.0 at.% SiO_2 and (d) 3.0 at.% SiO_2. Scale bar = 10 µm.

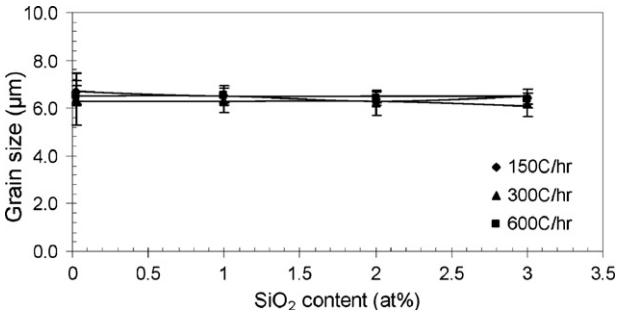

Fig. 2. Graphs showing the variation in grain size with SiO_2 content for each cooling rate.

2. Experimental

The thermistor samples used in this study were prepared from (Ba,Ca)TiO_3, doped with a rare earth donor and 0.1 at.% Mn acceptor. Samples were prepared with four different SiO_2 levels by including 0, 1.0, 2.0 and 3.0 at.% SiO_2. Each batch was placed in a polyethylene container with Mg-PSZ grinding media, using a powder to media ratio of 1:1. Isopropyl alcohol [$(CH_3)_2CHOH$] was added at an appropriate level to form a thin slurry, and the mixtures were milled in a vibratory mill for 18 h, followed by drying for 6 h at 85 °C in air. Disc compacts, 10 mm diameter and 2.2 mm thick, were pressed at a pressure of 8 kg mm^{-2}. Green pellets were sintered in air in a muffle furnace at a peak temperature of 1330 °C for 1 h with cooling rates of 150, 300 and 600 °C h^{-1}, producing sintered pellets 8 mm in diameter and 2 mm in thickness.

The sintered pellets were cleaned thoroughly in acetone, and In–Ga (2:1) eutectic alloy electrodes were applied to form ohmic contacts. Low field resistivity measurements were carried out in the temperature range 30–300 °C, at 10 °C intervals, by employing a two probe DC technique using a KEITHLEY 487 Picoammeter with a built-in voltage source. Samples were held at temperature for 30 min before each measurement to ensure thermal equilibration. Resistivity was calculated at each temperature using the average of 10 measurements.

Impedance measurements were carried out on samples approximately 1 mm thick and 8 mm diameter using a HP3192A

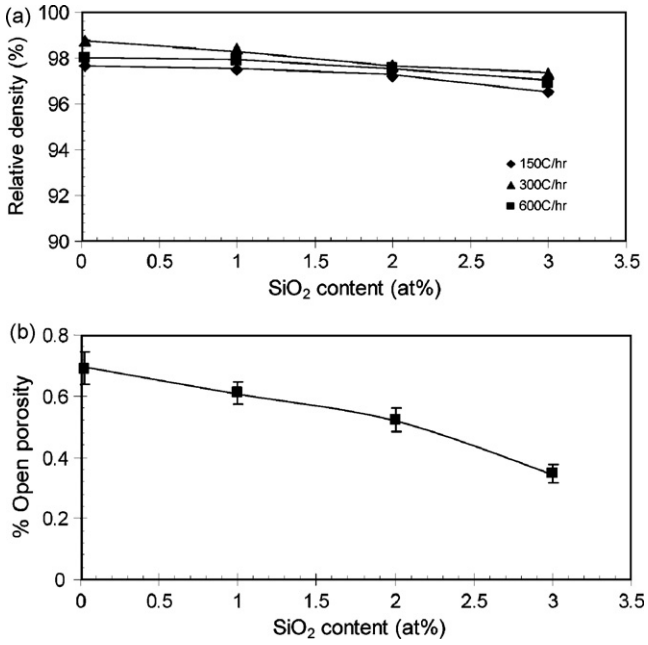

Fig. 3. Graphs showing (a) relative density as a function of SiO_2 content, compensated for SiO_2 content, and (b) open porosity as a function of SiO_2 content.

impedance analyser, operating over a frequency range of 5 Hz to 13 MHz. Data were collected in the temperature range 30–450 °C, at 10 °C intervals. Samples were held at temperature for 30 min prior to each measurement in order to ensure thermal equilibration. The real and imaginary components of impedance were obtained as a function of frequency and temperature, and were corrected for the effects of the sample holder and leads.

Microstructural analysis was carried out on polished cross-sections of the specimens using backscattered electron (BS) imaging in a Phillips XL30 FEGSEM operating at 10 kV. The average grain size was measured using the linear intercept method with a k value of 1.6. Sample density and porosity was measured using the Archimedes' method and compared with the theoretical density of (Ba,Ca)TiO_3 after compensating for SiO_2 addition. X-ray diffraction was carried out using a Phillips

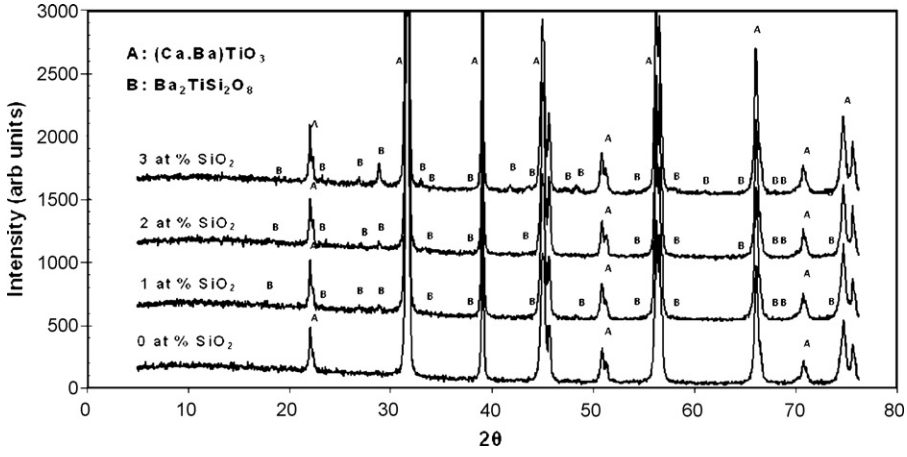

Fig. 4. XRD of samples as a function of SiO_2 content. Peaks labelled 'A' and 'B' are attributed to (Ca,Ba)TiO_3 and $BaTiSi_2O_8$, respectively.

X'pert APD Diffractometer, operating at 60 kV and 4 mA, fitted with PC-APD diffraction software. The samples were scanned over a 2θ range of 5–95°, using a 0.05° step scan.

3. Results and discussion

3.1. Microstructure

The microstructures of the samples cooled at 300 °C h^{-1} are shown in Fig. 1a–d, for each SiO_2 level. A SiO_2-rich second phase is predominantly observed at triple junctions, and is visible in all samples containing at least 1 at.% SiO_2, suggesting the presence of a transient liquid phase during sintering. As the SiO_2 is increased, the proportion of triple junctions appearing to contain a secondary silicate phase increases. Additionally, the predominant grain shape changes from rounded to {1 0 0} habit, indicating that the relative energies of different $BaTiO_3$ surfaces are modified by the presence of excess SiO_2, although the mean grain size remains largely unchanged (Fig. 2). Similar microstructures were observed in samples cooled at 150 and 600 °C h^{-1}.

The densities of the samples, when corrected for SiO_2 content, all lie in the range 96.5–98.5%, and decrease with increasing SiO_2 (Fig. 3a). Due to the lower density of silicate compared with (Ba,Ca)TiO_3, the titanate grain structure becomes progressively more 'open' as SiO_2 increases, i.e. for the samples with 0 at.% SiO_2 addition the titanate grains are more closely packed with a few pores trapped at the grain boundaries or triple points, but with increasing SiO_2 the apparent grain-to-grain contact area decreases. The proportion of open porosity was calculated as a function of SiO_2 addition, using the Archimedes' method, and was found to decrease smoothly from 0.70 ± 0.05% to 0.35 ± 0.03% as the SiO_2 level increased from 0 to 3 at.% (Fig. 3b).

XRD analysis (Fig. 4) identified the second phase as fresnoite, $Ba_2TiSi_2O_8$. The volume of fresnoite in the microstructure increases with SiO_2 addition, and appeared slightly more abundant in the more rapidly cooled samples.

In Ti-rich $BaTiO_3$ the formation of a $Ba_6Ti_{17}O_{40}$ second phase is widely reported, formed by the reaction of $BaTiO_3$ with excess TiO_2. [17] This phase is also reported to form in samples containing SiO_2 additions, along with a slightly Ba-rich fresnoite, according to the following reaction[17]:

$$28BaTiO_3 + 22SiO_2 \Leftrightarrow 11Ba_2TiSi_2O_8 + Ba_6Ti_{17}O_{40} \quad (4)$$

However, although fresnoite was observed in our samples, no $Ba_6Ti_{17}O_{40}$ was detected.

3.2. Electrical properties

Fig. 5a shows typical $\rho(T)$ curves for thermistors cooled at 150 °C h^{-1}, as a function of SiO_2 content, while Fig. 5b shows $\rho(T)$ curves for thermistors containing 1% SiO_2, as a function of cooling rate. Similar relationships between the $\rho(T)$ curves were seen for other cooling rates and SiO_2 additions. Increasing the SiO_2 content or the sample cooling rate decreased the room temperature resistivity, ρ_{25}, and the maximum resistivity, ρ_{max}, while reducing the gradient of the PTC portion of the $\rho(T)$ curve, and increasing the temperature of maximum resistivity, $T\rho_{max}$.

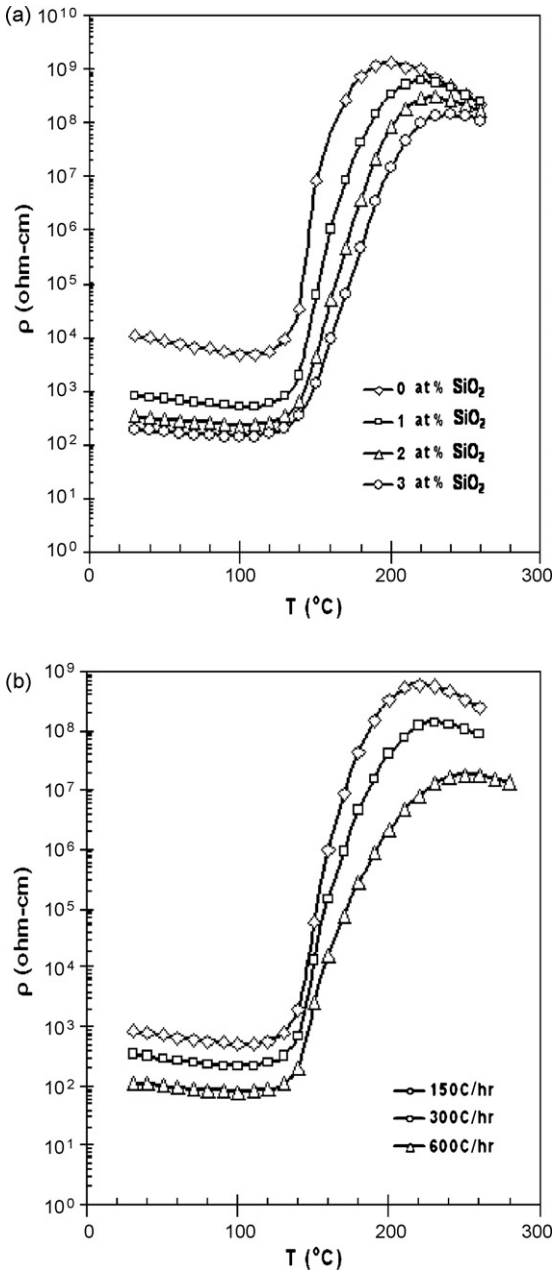

Fig. 5. $\rho(T)$ curves as a function of (a) SiO_2 content for samples cooled at 150 °C h^{-1} and (b) cooling rate for samples containing 1 at.% SiO_2.

Fig. 6a and b shows the variations in ρ_{RT} and ρ_{max}, respectively, as a function of cooling rate, and SiO_2 level, for all samples. The rate of variation increases as the SiO_2 level is reduced. Additionally, the rate of increase of ρ_{25} and ρ_{max} with decreasing cooling rate decreases as the amount of SiO_2 added to the starting powder is increased.

It is well known that the addition of acceptor impurities, such as manganese, increases the magnitude of the resistivity jump (ρ_{max}/ρ_{25}), [20,21] through the compensation of Mn''_{Ti} substitutional defects by oxygen vacancies, $V_0^{\bullet\bullet}$, in order to maintain

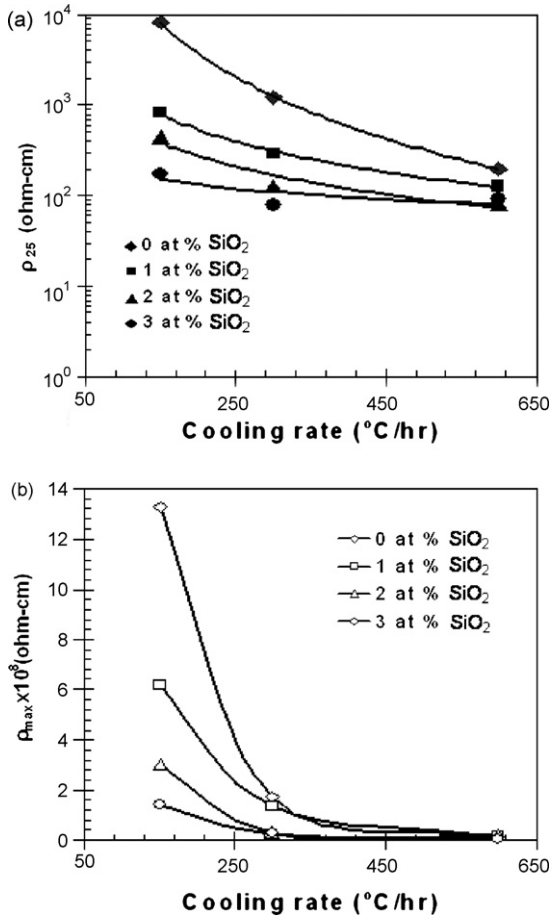

Fig. 6. Variation in (a) ρ_{25} and (b) ρ_{max} with cooling rate for each SiO_2 content.

overall charge neutrality, according to:

$$MnO \xrightarrow{TiO_2} Mn''_{Ti} + O^x_O + V_O^{\bullet\bullet} \quad (5)$$

During reoxidation on cooling, oxygen vacancies are lost and the Mn-ions at the grain boundaries form acceptor states.[22] Thus, during reoxidation $N_S(T)$ increases, leading to an associated increase in $\varphi_0(T)$, according to Eq. (2). Extending the time available for reoxidation, e.g. by decreasing cooling rate, allows for a greater increase in $N_S(T)$, giving rise to a bigger PTC resistivity jump. Changes in PTC curve position and shape with cooling rate are therefore explained simply in terms of changes in time available, and hence the extent of reoxidation during cooling.

A variation in curve position with increasing SiO_2 content, similar to that observed for an increase in cooling rate, occurred within our samples. This can be understood in terms of microstructural changes since with increasing addition of SiO_2 the proportion of triple junctions occupied by fresnoite increases and the amount of open porosity progressively decreases. Both these observations imply a reduction in available pathways for oxygen migration within the thermistor, and hence reoxidation during cooling. This is illustrated schematically in Fig. 7a–d. There is also the possibility that the increased volume of secondary phase in the high SiO_2 samples will dissolve more Mn during sintering, reducing the concentration of Mn available for

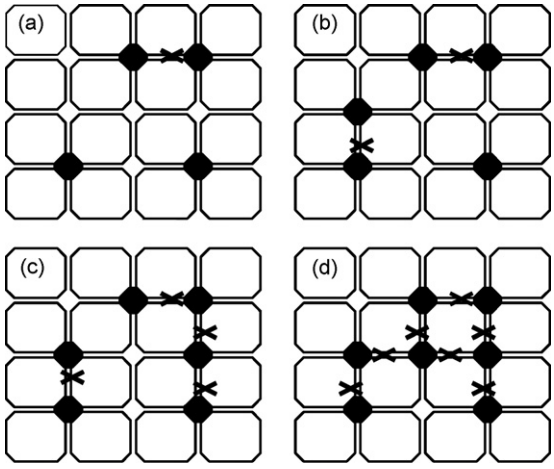

Fig. 7. (a–d) Schematic diagram showing a progressive increase in the proportion of blocked grain boundaries (crosses) with increasing triple point second phase (spots).

acceptor state formation. However, we were unable to confirm this through TEM analysis due to the low concentration of Mn present. All of these processes would reduce $N_S(T)$, reducing both the residual barrier below T_C and the interface potential barrier above T_C, leading to reductions in resistivity in both regions. Previous workers[17] have discussed a similar variation in ρ_{25} with SiO_2 addition in terms of increased fresnoite content, which prevents the formation of Ba-vacancies by inhibiting the reaction between BaO and $Ba_6Ti_{17}O_{40}$ to form $BaTiO_3$. Since no $Ba_6Ti_{17}O_{40}$ was observed in our samples, the mechanism they describe is unlikely in our case.

Thus, for a given composition, the position and shape of the PTC curve simply reflects the extent of grain boundary oxidation in the material, and is influenced both by cooling rate and SiO_2

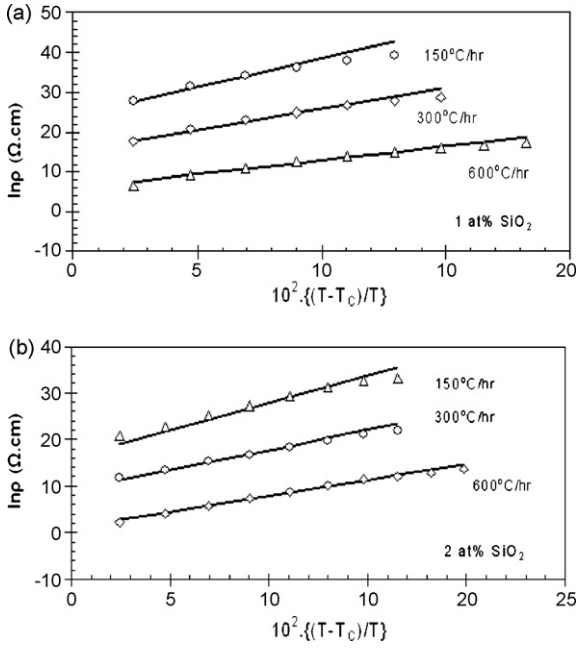

Fig. 8. Arrhenius plots for each cooling rate in samples containing (a) 1.0 at.% SiO_2 and (b) 2.0 at.% SiO_2.

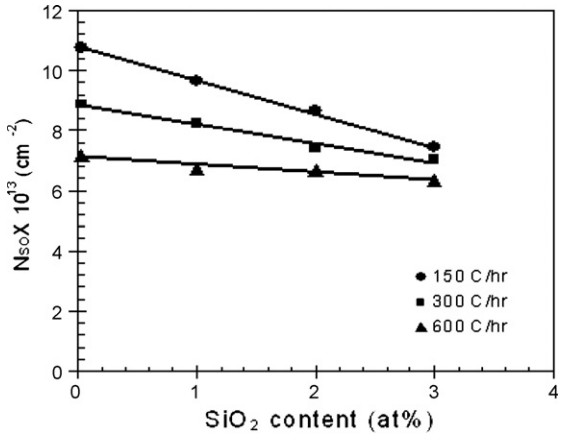

Fig. 9. Effect of cooling rate and SiO_2 content on the variation in surface state density, calculated from the Arrhenius plots.

level. We also note that the effect of cooling rate on ρ_{25} and ρ_{max} is observed to be more significant at low SiO_2 levels (Fig. 6), possibly reflecting the importance of open oxygen migration pathways on the reoxidation kinetics.

According to the DSB model[1] the initial gradient of the $\rho(T)$ curve, $d\rho/d(1 - T_C/T)$, just above T_C should remain constant provided the occupied acceptor state density remains unaffected by the relative shift of surface state energy level with respect to the Fermi level inside the forbidden zone and the relative permittivity varies according to the Curie–Weiss law. On this basis, combining Eqs. (1)–(3) gives:

$$\rho_L = R_0 \exp\frac{e^2(N_S(T))^2(T - T_C)}{8\varepsilon_0 C k N_d T} \quad (6)$$

At temperatures near T_C all the acceptor states are fully occupied,[7,19] and so, $N_S(T)$ is equal to the total activated surface state density N_{SO}. As a result ρ_L increases rapidly with

Table 1
Values of surface state density and energy, extracted from ρ_{max}–T_{max} plots and Arrhenius plots for a single value of E_S

Cooling rate (°C h^{-1})	SiO_2 content (at.%)	Single acceptor energy		N_{SO} (cm^{-2}) from Arrhenius graphs
		N_{SO} (cm^{-2})	E_S (eV)	
150	0	1.09×10^{14}	1.51	1.08×10^{14}
	1.0	0.97×10^{14}	1.54	0.97×10^{14}
	2.0	0.92×10^{14}	1.55	0.86×10^{14}
	3.0	0.86×10^{14}	1.55	0.74×10^{14}
300	0	0.95×10^{14}	1.49	0.89×10^{14}
	1.0	0.90×10^{14}	1.51	0.83×10^{14}
	2.0	0.80×10^{14}	1.51	0.74×10^{14}
	3.0	0.77×10^{14}	1.53	0.71×10^{14}
600	0	0.82×10^{14}	1.58	0.72×10^{14}
	1.0	0.77×10^{14}	1.55	0.67×10^{14}
	2.0	0.76×10^{14}	1.57	0.67×10^{14}
	3.0	0.71×10^{14}	1.58	0.64×10^{14}

Table 2
Values of surface state density and energy, extracted from ρ_{max}–T_{max} plots for different values of Δ

Cooling rate (°C h^{-1})	SiO_2 content (at.%)	Acceptor energy spread (eV)					
		0.25		0.5		0.75	
		N_{SO} (cm^{-2})	E_S (eV)	N_{SO} (cm^{-2})	E_S (eV)	N_{SO} (cm^{-2})	E_S (eV)
150	0	1.11×10^{14}	1.55	1.16×10^{14}	1.60	1.37×10^{14}	1.58
	1.0	0.98×10^{14}	1.57	1.01×10^{14}	1.65	1.08×10^{14}	1.69
	2.0	0.92×10^{14}	1.58	0.94×10^{14}	1.65	0.98×10^{14}	1.71
	3.0	0.87×10^{14}	1.59	0.88×10^{14}	1.66	0.91×10^{14}	1.73
300	0	0.96×10^{14}	1.52	0.98×10^{14}	1.60	1.06×10^{14}	1.63
	1.0	0.91×10^{14}	1.55	0.93×10^{14}	1.62	0.97×10^{14}	1.68
	2.0	0.81×10^{14}	1.55	0.82×10^{14}	1.62	0.84×10^{14}	1.70
	3.0	0.77×10^{14}	1.57	0.78×10^{14}	1.65	0.80×10^{14}	1.73
600	0	0.82×10^{14}	1.58	0.83×10^{14}	1.65	0.85×10^{14}	1.73
	1.0	0.76×10^{14}	1.55	0.77×10^{14}	1.62	0.79×10^{14}	1.70
	2.0	0.76×10^{14}	1.57	0.77×10^{14}	1.65	0.78×10^{14}	1.73
	3.0	0.71×10^{14}	1.58	0.72×10^{14}	1.66	0.73×10^{14}	1.74

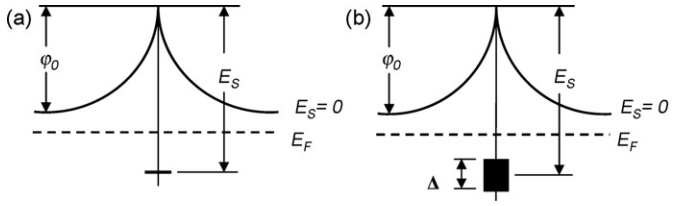

Fig. 10. A schematic band diagram for the interface potential barrier with acceptor levels, (a) concentrated in a single energy state and (b) continuously distributed within an energy range of Δ.

temperature above T_C. Eq. (6) can be written in Arrhenius form:

$$\ln \ \rho_L = A\left(\frac{T - T_C}{T}\right) + \ln \ R_0 \tag{7}$$

where A is a constant, representing the gradient of the Arrhenius plot. Hence:

$$N_{SO} = \sqrt{\frac{8Ak\varepsilon_0 C N_d}{e^2}} \tag{8}$$

Two typical examples of Arrhenius plots are shown in Fig. 8 for which a T_C of 130 °C was used. There is some deviation of the experimental points from linearity at higher temperatures, which is due to the effect of depopulation of surface states as they approach the Fermi level. Values of N_{SO}, calculated from the initial gradients using Eq. (8), with respect to SiO_2 and cooling rate, are presented in the final column of Table 1 and in Fig. 9. In these calculations, a value of N_d of $1.41 \times 10^{18}\,cm^{-3}$ was used, being obtained from the highest frequency intercept in a complex impedance plot in the usual way. It can be seen from these curves that the surface state density gradually increases with a decrease in either cooling rate or SiO_2 content, which is consistent with the explanation for variation in curve position given earlier.

3.3. Theoretical analysis

For a polycrystalline thermistor with z grains cm^{-1} between the electrodes, the effective resistivity including the interface potential barrier is given by[2]:

$$\rho(T) = \left(\frac{1}{N_d e \mu}\right)\left[1 + \left\{\frac{zb(T)kT}{e\varphi(T)}\right\}\exp\left\{\frac{e\varphi(T)}{kT}\right\}\right] \tag{9}$$

where, $b(T)$ is the barrier layer width, given by $\{N_S(T)\}/(2N_d)$, and μ is the electron mobility, here taken a $0.5\,cm^2\,Vs^{-1}$. The value for z was based on an average sample grain size of 6.4 μm.

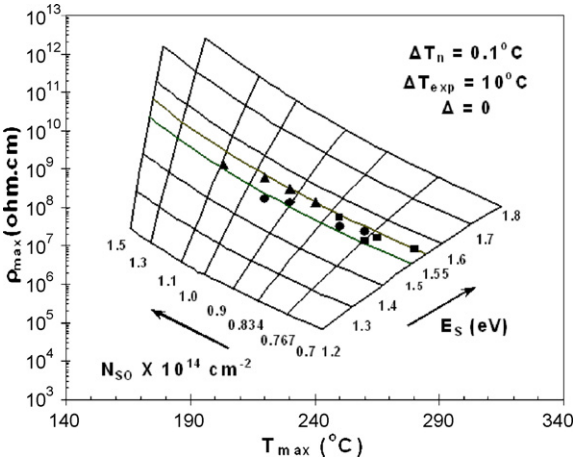

Fig. 11. ρ_{max}–T_{max} plots for a single energy state.

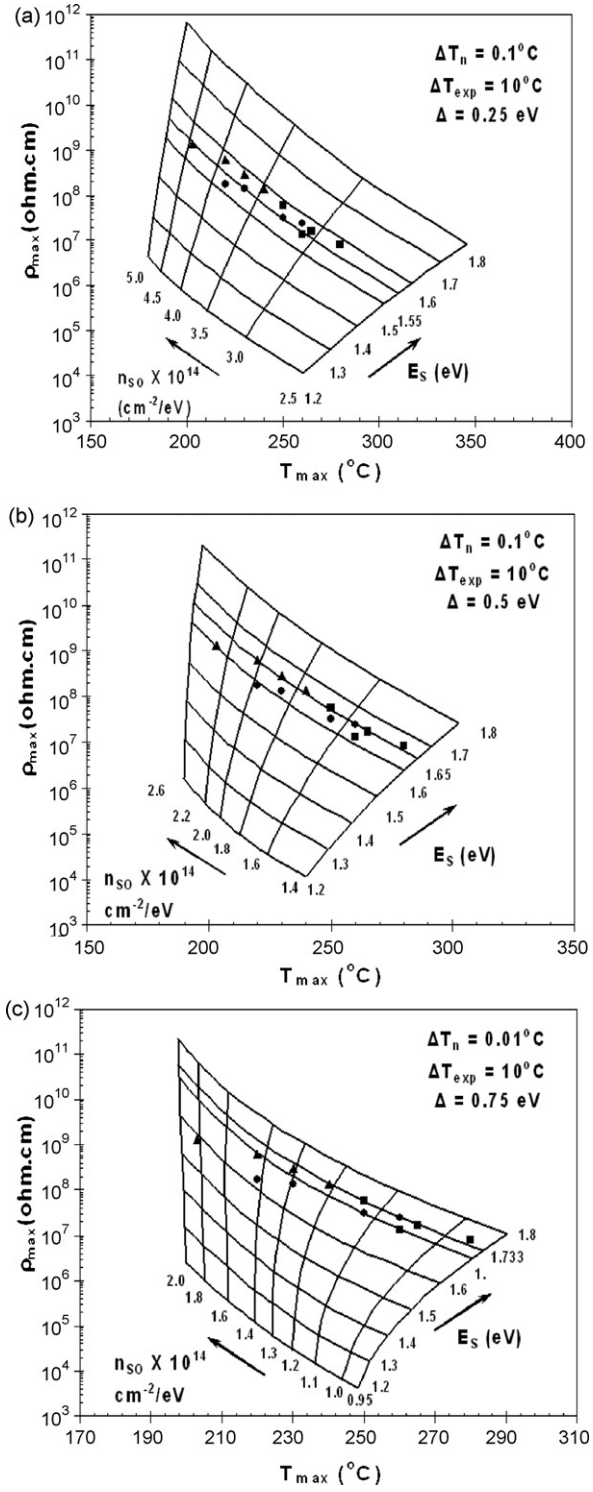

Fig. 12. ρ_{max}–T_{max} plots for (a) $\Delta = 0.25$ eV, (b) $\Delta = 0.5$ eV and (c) $\Delta = 0.75$ eV.

The value of $N_S(T)$ can be represented in the form of a Fermi distribution function[1,2]:

$$N_S(T) = \frac{N_{SO}}{1 + \exp\{E_F + e\varphi(T) - E_S/kT\}} \quad (10)$$

where, E_S = energy of grain boundary acceptor levels below the conduction band edge, assuming all acceptors are concentrated in a single energy state within the forbidden zone (Fig. 10a). E_F is the Fermi energy, which is given by;

$$E_F = kT \ \ln\left(\frac{N_0}{N_d}\right) \quad (11)$$

where, N_0 = density of states, taken as 1.56×10^{22} cm^{-3}, corresponding to the density of Ti ions.[23–25].

In order to model the $\rho(T)$ characteristics, the total surface state density, N_{SO}, and the surface state energy, E_S, were established for each sample by solving Eqs. (2) and (10) for a constant value of effective donor concentration using a Newton–Raphson technique and assuming Curie–Weiss behaviour. The calculations were repeated for several values of surface state density and acceptor depth, and then over a range of temperatures above T_C to obtain values of effective, or occupied, trap densities and barrier heights as a function of temperature. Values of ρ_{max} and T_{max} were extracted using Eq. (9) for a constant trap density and trap energy levels in the range 1.2–1.8 eV. Then a ρ_{max}–T_{max} plot was constructed as a function of effective surface state density and surface state energy, in the manner described by Jonker.[18] Our experimental ρ_{max} and T_{max} data were superimposed on this plot to extract the values of N_{SO} and E_S as a function of SiO_2 content and cooling rate (Fig. 11). These values are listed in Table 1. It can be seen that N_{SO} decreases with an increase in either the SiO_2 content or cooling rate. Values of N_{SO} obtained from the ρ_{max}–T_{max} plots are close to those obtained from the Arrhenius plots, also listed in Table 1. Our values of E_S all

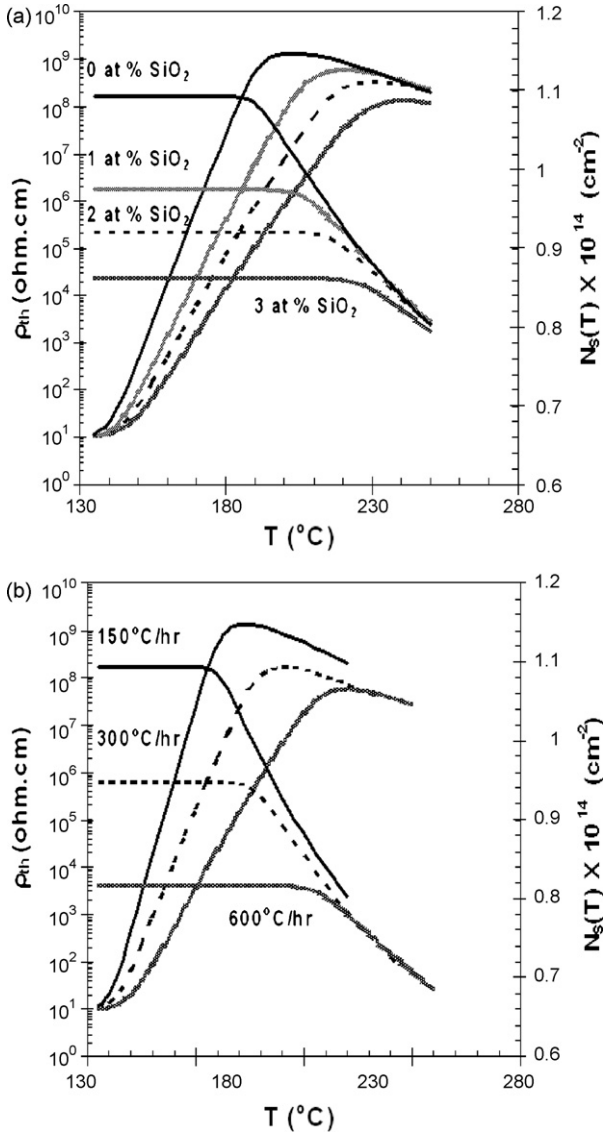

Fig. 13. Calculated values of resistivity and $N_S(T)$ as a function of temperature for (a) four different SiO_2 contents an (b) three different cooling rates.

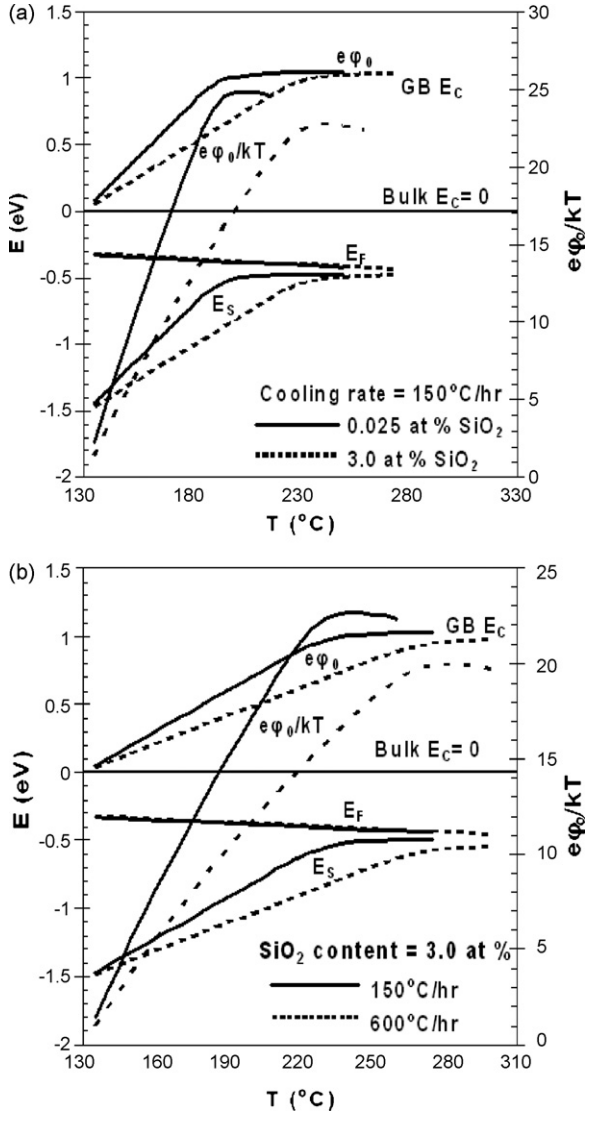

Fig. 14. Calculated values of PTC shape factor ($e\varphi_0/kT$) and interface potential barrier height ($e\varphi_0$) to illustrate Fermi pinning as a function of (a) SiO_2 content and (b) cooling rate.

fall within the range 1.51–1.55 eV, which is slightly higher than other published values for Mn-doped $BaTiO_3$ PTC thermistors (1.40–1.47 eV).[22] We believe this discrepancy is consistent with differences between the two sets of samples: our Mn-doped (Ba,Ca)TiO_3 samples exhibit a higher ρ_{max} (10^7–$10^9\ \Omega$ cm) than those in the previously published study (10^5–$10^8\ \Omega$ cm), although values of T_{max} are similar (220–280 °C).

Values of total surface state density and acceptor energy depth were also calculated for the case where there is a continuous distribution of acceptor states, spread over a narrow energy range, Δ, centred on E_S, as shown schematically in Fig. 10b, using the analysis proposed by Ihring and Puschert.[19] A constant number of states per unit area and unit energy n_{so} is also assumed for simplicity. Using these assumptions, Eq. (10) is modified to[19]:

$$N_S(T) = n_{SO}kT\left[\frac{\Delta}{kT} - \ln\frac{1+\exp\{e\varphi(T)+E_F-E_S+(1/2)\Delta/kT\}}{1+\exp\{e\varphi(T)+E_F-E_S-(1/2)\Delta/kT\}}\right] \quad (12)$$

ρ_{max}–T_{max} plots were constructed in a similar fashion for Δ values of 0.25, 0.5 and 0.75 eV as a function of n_{so} and E_S and are presented in Fig. 12a–c. The experimental ρ_{max} and T_{max} data were superimposed on each of the ρ_{max}–T_{max} plots in order to extract corresponding values of N_{SO} and E_S for our samples as a function of Δ, cooling rate and SiO_2 content (Table 2). Increases in SiO_2 or cooling rate both reduce N_{SO} irrespective of Δ. The gradual shift in surface state energy levels towards higher values with increasing Δ may partly be due to a reduction in the energy difference between the Fermi level and the upper edge of the distributed surface states band, which will automatically increase E_S, provided the temperature difference between T_C and $T\rho_{max}$ is fixed.

Fig. 13a and b shows the calculated values of resistivity and $N_S(T)$ as a function of SiO_2 content and cooling rate. Fig. 14a and b shows the relation between E_F, the interface conduction band edge energy, GBE_C, and the acceptor energy level in the forbidden zone with respect to temperature. The resistivity reaches a maximum value at a temperature near to the onset of depopulation of surface states. The temperature at which depopulation starts increases with both SiO_2 content and cooling rate. By

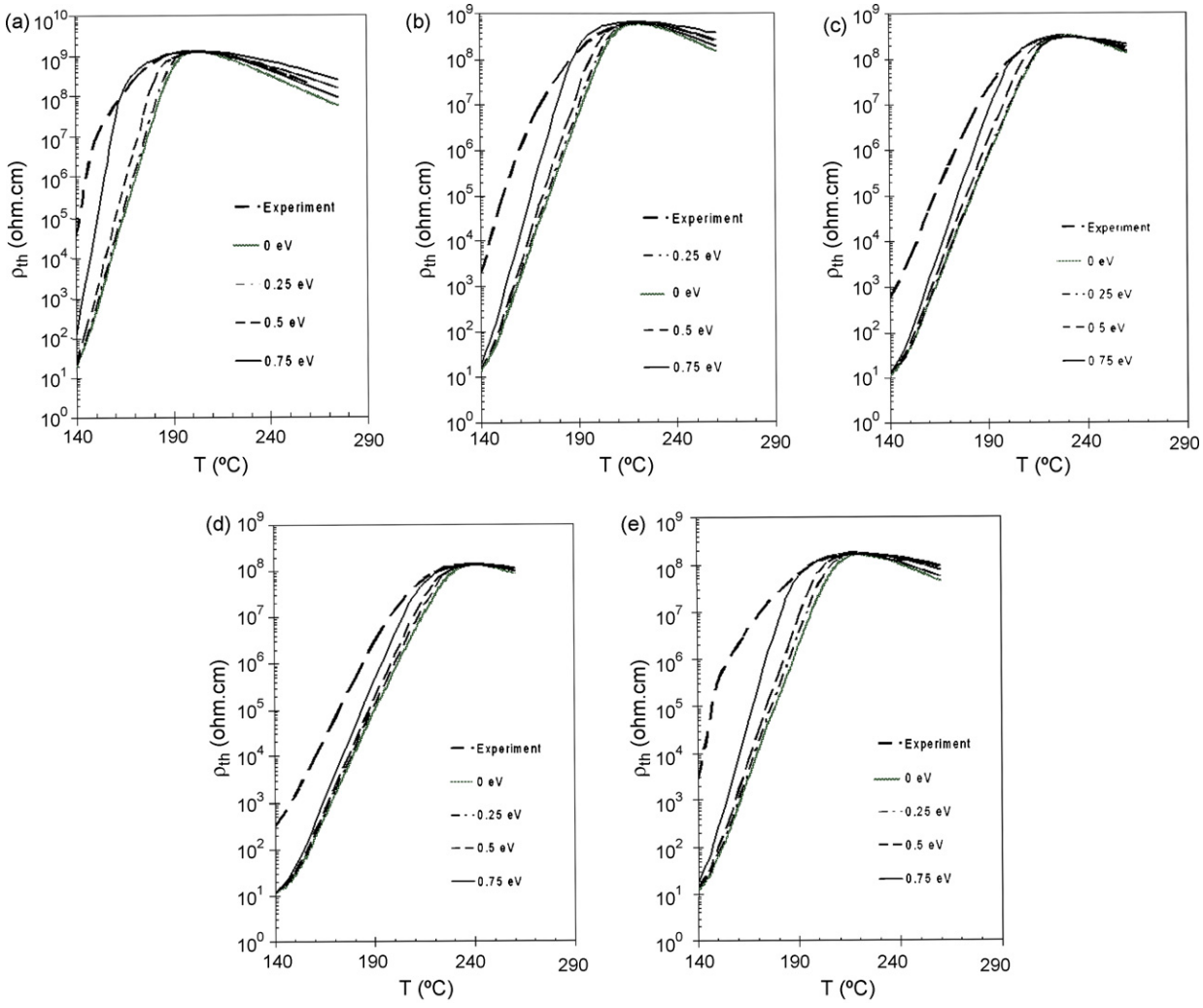

Fig. 15. Comparison between the theoretical and experimental ρ–T characteristics for four different values of Δ for samples with (a) 0 at.% SiO_2, 150 °C h^{-1}, (b) 1.0 at.% SiO_2, 150 °C h^{-1}, (c) 2.0 at.% SiO_2, 150 °C h^{-1}, (d) 3.0 at.% SiO_2, 150 °C h^{-1} and (e) 0 at.% SiO_2, 300 °C h^{-1}.

comparing Figs. 13a and 14a it can be seen that surface state depopulation begins when the surface state energies approach the Fermi level due to the rise in interface potential barrier height with increase in temperature. Since the interfacial potential barrier increases more slowly in the samples with the higher SiO_2 content, Fermi pinning and consequently the depopulation of surface states is delayed, resulting in a higher value of $T\rho_{max}$. Comparison of Figs. 13b and 14b shows that an increase in cooling rate also shifts the onset of Fermi pinning, and hence the temperature corresponding to onset of surface state depopulation, to higher temperatures. This is achieved through a reduction in the rate of rise of the interface potential barrier with respect to temperature ($d\varphi_0/dT$), in a similar manner to that for increasing SiO_2 content. The reduction in $d\varphi_0/dT$ is therefore solely due to a reduction in N_{SO}.

$\rho(T)$ characteristics were calculated using the parameters tabulated in Tables 1 and 2, for a range of Δ, and compared with the experimental $\rho(T)$ curves from our samples (Fig. 15a–e). As Δ increases the discrepancy between the calculated and the experimental curves gradually decreases for all SiO_2 levels and cooling rates, especially within the high temperature NTC region and just below $T\rho_{max}$. For low values of Δ the calculated resistivity peak is quite sharp, whereas for Δ values between 0.5 and 0.75 eV $d\rho/dT$ the resistivity change with respect to temperature around $T\rho_{max}$ broadens with a larger initial PTC slope and hence a larger value of N_{SO} and there is better agreement between theory and experiment around peak resistivity and within the NTC region. The residual discrepancy is attributed to an overestimate of the permittivity of the grain boundary layer through the use of the Curie–Weiss law, and is supported by the observation that lower permittivity values have been calculated from single grain boundary capacitance measurements,[26] together with evidence that grain boundary defects and internal stresses can also reduce the actual permittivity above T_C.[19] An additional factor affecting the fit may be the simplistic assumption of a continuous distribution of acceptor states and a constant density of states per unit energy n_{so}, given the coexistence of Ba-vacancies, impurities and dopants.[19]

4. Summary

Co-doped (Ba,Ca)TiO_3 based PTC thermistor samples were prepared with additions of 0, 1.0, 2.0 and 3.0 at.% SiO_2 and with cooling rates of 150, 300 and 600 °C h^{-1}. An increase in SiO_2 content was found to decrease the sample density, reduce grain-to-grain contact area, decrease the volume fraction of open porosity and increase the proportion of silicate second phase present at triple junctions.

SiO_2 has long been added to $BaTiO_3$ as a sintering aid, but has not been reported to affect significantly the electrical properties of PTC thermistors. In this systematic study we have observed that additions of SiO_2 and increases in sample cooling rate both modify the electrical characteristics by decreasing ρ_{25}, ρ_{max} and $d\rho/dT$, whilst displacing $T\rho_{max}$ towards higher temperatures. Variations in SiO_2 content and cooling rate were not found to affect the bulk resistivity.

The variation in low field $\rho(T)$ behaviour was analysed as functions of SiO_2 content and cooling rate over the full range of the PTC transition using two different models, one based on an Arrhenius analysis and the other on direct modelling of ρ–T behaviour above T_C. It was observed for the first time that SiO_2 additions affect the interfacial electrical parameters, N_{SO} and E_S, in a way that is directly analogous to changes in cooling rate, both decreasing N_{SO}, while E_S remained unchanged within the range 1.51–1.55 eV. The consistency of data obtained using these two distinct models, both in terms of absolute values and variation with changes in composition and/or processing adds weight to this interpretation.

These systematic changes in electrical behaviour with SiO_2 addition were attributed to a reduction in activated acceptor state density in the grain boundary regions due to incomplete reoxidation caused by a progressive blocking of triple junctions and a reduction in open porosity, together with possible dissolution of Mn into an increasing volume of silicate phase during sintering.

The agreement between theoretical and experimental $\rho(T)$ characteristics was found to be poor when the surface state energy levels were confined to a single energy level. Agreement gradually improved, especially around $T\rho_{max}$ and in the high temperature NTC region, when the surface states were considered to be distributed over a broader energy range (Δ = 0.5–0.75 eV). A discrepancy between the calculated and experimental ρ–T curves between T_C and $T\rho_{max}$ may be due to the grain boundary layer having a lower permittivity than predicted by the Curie–Weiss law and complexity in the surface state distribution.

Acknowledgments

Financial support from the University of Manchester, ORS and GE Sensing is acknowledged.

References

1. Heywang, W., *J. Amer. Ceram. Soc.*, 1964, **47**, 484.
2. Jonker, G. H., *Solid State Electron.*, 1964, **7**, 895.
3. Jonker, G. H., Grain boundary phenomena in electronic ceramics. *Am. Ceram. Soc.*, 1981, 155.
4. Heywang, W., *J. Mater. Sci.*, 1971, **6**, 1214.
5. Kuwabara, M., *Solid State Electron.*, 1984, **27**, 929.
6. Daniels, J. and Wernicke, R., *Philips Res. Repts.*, 1976, **31**, 544.
7. IIIingsworth, J., Al-Allak, H. M. and Brinkman, A. W., *J. Phys. D: Appl. Phys.*, 1990, **23**, 971.
8. Hozer L, Semiconductor Ceramics: Grain Boundary Effects, Ellis Horwood, Polish Scientific Publishers PWN, 1994.
9. Ihring, H., *J. Am. Ceram. Soc.*, 1981, **64**, 617.
10. Park, M. B., Kim, C. D. and Cho, N. H., *Mater. Sci. Eng. B*, 2003, **99**, 15.
11. Ueoka, H., *Ferroelectrics*, 1974, **7**, 351.
12. Ting, C.-J., Peng, C.-J., Lu, H.-Y. and Wu, S.-T., *J. Am. Ceram. Soc.*, 1990, **73**, 329.
13. Rase, D. E. and Roy, R., *J. Am. Ceram. Soc.*, 1955, **38**, 389.
14. Roseman, R. D. and Mukharjee, N., *J. Electroceram.*, 2003, **10**, 117.
15. Ueoka, H. and Yodogana, M., *IEEE Trans. Manuf. Technol. MFT-3*, 1974, 77.
16. Cheng, H.-F., *J. Appl. Phys.*, 1989, **66**, 1382.
17. Abicht, H. P., Langhammer, H. T. and Felgner, K. H., *J. Mater. Sci.*, 1991, **26**, 2337.
18. Jonker, G. H., *Mater. Res. Bull.*, 1967, **2**, 401.

19. Ihring, H. and Puschert, W., *J. Appl. Phys.*, 1977, **48**, 3081.
20. Matsuoka, T., Matsuo, Y., Sasaki, H. and Hayakawa, S., *J. Am. Ceram. Soc.*, 1971, **55**, 108.
21. IIIingsworth, J., Al-Allak, H. M., Brinkman, A. W. and Woods, J., *J. Appl. Phys.*, 1990, **67**, 2088.
22. Allak, H. M., Brinkman, A. W., Russell, G. J. and Woods, J., *J. Appl. Phys.*, 1988, **63**, 4530.
23. Garthsen, P., Groth, R. and Hardtl, K. H., *Phys. Status Solidi*, 1965, **11**, 303.
24. Brzozowski, E. and Castro, M. S., *J. Eur. Ceram. Soc.*, 2004, **24**, 2499.
25. Ihring, H. and Hennings, D., *Phys. Rev. B*, 1978, **17**, 4593.
26. Gerthsen, P. and Hoffmann, B., *Solid State Electron.*, 1973, **16**, 617.